Suppression of superconductivity in $La_{1.85}Sr_{0.15}Cu_{1-y}Ni_yO_4$: The relevance of local lattice distortions

Daniel Haskel[*], Edward A. Stern[‡], Victor Polinger[‡] and Fatih Dogan[†]

[*] *Experimental Facilities Division, Advanced Photon Source, Argonne National Laboratory, Argonne IL 60439, USA*

[‡] *Department of Physics, Box 351560, University of Washington, Seattle WA 98195, USA*

[†] *Department of Materials Science and Engineering, Box 352120, University of Washington, Seattle WA 98195, USA*

Abstract.

The effect of Ni substitution upon the local structure of $La_{1.85}Sr_{0.15}Cu_{1-y}Ni_yO_4$ is commonly neglected when addressing the Ni-induced destruction of the superconducting state at $y \approx 0.03$ and a metal-insulator transition at $y \approx 0.05$. It is also sometimes assumed that direct substitution of a dopant into the CuO_2 planes has a detrimental effect on superconductivity due to in-plane lattice distortions around the dopants. We present here results from angular-dependent x-ray absorption fine structure (XAFS) measurements at the Ni, La and Sr K-edges of oriented powders of $La_{1.85}Sr_{0.15}Cu_{1-y}Ni_yO_4$ with $y = 0.01, 0.03, 0.06$. A special magnetic alignment geometry allowed us to measure pure $\hat{c}$ and $\hat{ab}$ oriented XAFS at the Ni K-edge in identical fluorescence geometries. Both the near-edge absorption spectra (XANES) and the XAFS unequivocally show that the NiO_6 octahedra are largely contracted along the c-axis, by $\approx 0.16\,\text{Å}$. Surprisingly, the Ni-O planar bonds and the Ni-O-Cu/Ni planar buckling angle are nearly identical to their Cu counterparts. The NiO_6 octahedral contraction drives the macroscopic $\hat{c}$-axis contraction observed with Ni-doping. The local $\hat{c}$-axis strongly fluctuates, due to the different NiO_6 and CuO_6 octahedral configurations and the much stronger bonding of a La^{+3} ion than a Sr^{+2} ion to the O(2) apical oxygens. We discuss the relevance of these findings to the mechanisms of T_c suppresion and hole-localization by Ni dopants.
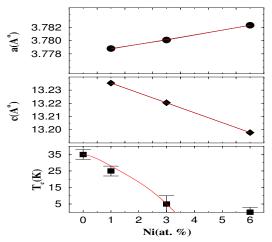
INTRODUCTION

At first it might seem a rather negative approach: to try to learn about super-conductivity by destroying it with Ni doping. However, the work of Pan *et al.* demonstrated just the opposite [1]. In their scanning tunneling microscopy (STM) experiments on T_c-suppressed Zn doped $Bi_2Sr_2CaCu_2O_8$ at temperatures below T_c, no quasiparticle tunneling current was obtained at zero bias for most of the STM tip locations on the cleaved BiO surface, as expected due to the presence of a su-perconducting gap. However, a zero-bias tunneling current was measured when the STM tip was located precisely above a Zn dopant (two layers below the BiO surface) indicating a "metallic" or un-gapped state at the Zn dopant sites. By mapping the spatial extent of the Zn impurity-state away from its lattice site in different direc-tions (by measuring the tunneling strength as function of tip displacement away from the dopant), a *d*-wave like dependence was obtained, the impurity-state ex-tending the furthest along the *nodes* of the SC gap. This spatial dependence agrees with theoretical predictions [2,3]. However, an additional, weaker, tunneling signal with spatial extent that corresponds to an impurity state extending *along* the SC gap was also detected. It was proposed that this weaker signal is due to enhanced tunneling between layers along the Cu-O bond directions [3].

It is clear that the local structure around dopants will influence the nature of the impurity states. Electronic states at the Fermi level are derived from O 2p and Cu 3d atomic orbitals, which are largely affected by deviations in local symme-try through crystal-field splittings. Local distortions around dopants (and related changes in local electronic structure) will affect the tunneling matrix elements at a dopant site, compared to that at a neighboring Cu site. It is therefore of impor-tance to obtain detailed information on the local environment of the dopants when interpreting information from other spectroscopies at the atomic level. It is inter-esting to note that doping Zn or Ni into the CuO_2 planes of SC cuprates have very similar effects: both contract the crystallographic $\hat{c}$-axis and suppress T_c, although Zn does the latter at a faster rate. In $La_{1.85}Sr_{0.15}Cu_{1-y}Ni_yO_4$, SC is destroyed at $y \approx 0.03$ and a M-I transition takes place at $y \approx 0.05$ [4].

EXPERIMENTAL

Powders of $La_{1.85}Sr_{0.15}Cu_{1-y}Ni_yO_4$ with $y = 0.01, 0.03, 0.06$ were obtained from nitrates by precipitation from solution [5]. Sintering of powder compacts (≈ 3 grams) took place at $1140°C$ for 24 hours. Lattice parameters were refined at room temperature using 14 Bragg reflections of the *I4/mmm* space group. Supercon-ducting T_c's were obtained from zero field cooled magnetization curves measured by SQUID magnetometry in a H=1 Gauss applied field. Figure 1 shows the results from these measurements.

Angular resolved XAFS measurements were taken on magnetically aligned pow-ders. A general description of the alignment procedure is described in ref 5. This
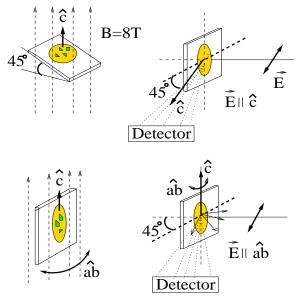
FIGURE 1. Room temperature lattice parameters and T_c's for $La_{1.85}Sr_{0.15}Cu_{1-y}Ni_yO_4$. The value of T_c at $y = 0$ is from Radaelli *et al.* [6]

procedure results in powders align along their $\hat{c}$-axis but randomly oriented in the $\hat{ab}$-plane. The main advantage of this method over the use of single crystals is control over sample thickness, allowing the use of transmission geometry at the absorption edges of concentrated elements. It also allows controlling the orientation of the $\hat{c}$-axis relative to the sample's surface. The latter allowed us to measure pure $\hat{c}$-axis and $\hat{ab}$-plane orientations at the Ni K-edge in identical fluorescence geometries (Fig. 2). Measurements were done in fluorescence at the Ni K-edge and transmission at the Sr, La K-edges at beamline X11-A of the National Synchrotron Light Source using Si(111) (Ni, Sr K-edges) and Si(311) (La K-edge) double crystal monochromators. Ni K-edge XAFS is limited to about $\approx 13\,\text{Å}^{-1}$ due to the appearance of Cu K-edge in the absorption spectra.
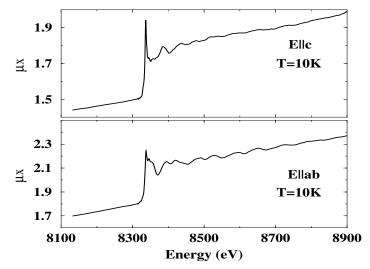
Absorption spectra at the Ni K-edge of $La_{1.85}Sr_{0.15}Cu_{1-y}Ni_yO_4$ with $y = 0.06$ are shown in Fig. 3 for both orientations of the electric field. Fig. 4 emphasizes the near-edge region of the same spectra.

ANALYSIS AND RESULTS

Data analysis was carried out with the UWXAFS analysis package [7] together with theoretical standards from FEFF6 [8]. The orientation dependence of the XAFS signal was included in the FEFF6 calculation by performing the appropiate angular averaging for powder aligned along the $\hat{c}$-axis but randomly oriented in the $\hat{ab}$-plane. Data from both electric field orientations are analyzed concomitantly by constraining the structural parameters of scattering paths that contribute in both orientations, significantly reducing the number of fitting parameters relative to the number of independent points in the data. Coordination numbers were set to the values of the average structure determined by crystallography for undoped $La_{1.85}Sr_{0.15}CuO_4$ [6]. Figure 5 shows fit results at the Ni K-edge for both electric
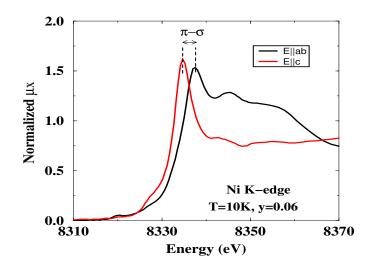
FIGURE 2. Magnetic alignment geometry. Having the crystallographic $\hat{c}$-axis forming 45° with the sample surface allowed measuring pure c-axis Ni K-edge fluorescence ($\hat{E} \parallel \hat{c}$) with the sample surface forming 45° with the x-rays' electric field (top panel). For the $\hat{E} \parallel \hat{ab}$ fluorescence measurements at the Ni K-edge (and transmission measurements in both orientations at the Sr an La K-edges) samples were aligned with the $\hat{c}$-axis in the plane of the sample (bottom panel)
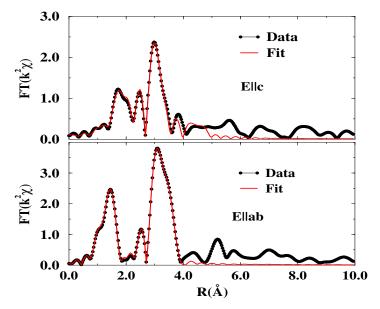

FIGURE 3. Ni K-edge absorption spectra for $y = 0.06$ measured in fluorescence geometry with $\hat{E} \parallel \hat{c}$ (top) and $\hat{E} \parallel \hat{ab}$ (bottom) orientations.

field orientations. Fits are performed in real-space and multiple scattering (MS) paths that contribute to the XAFS in the fitted region are included in the fits.

Structural parameters derived from the fits in Fig. 5 are summarized in Table 1.

FIGURE 4. Orientation-dependent near-edge structure (XANES) at the Ni K-edge. The $4p_\pi$-$4p_\sigma$ energy splitting is determined by the distortion of the NiO$_6$ octahedron.

FIGURE 5. Magnitude of the complex Fourier transform of $k^2\chi(k)$ for Ni K-edge in La$_{1.85}$Sr$_{0.15}$Cu$_{1-y}$Ni$_y$O$_4$ with $y = 0.06$ at T=10K. The k-range used in the transform is [2.5-12.0] Å^{-1}. Number of fitting parameters in the constrained fit of both orientations is 16, compared to a total of 45 independent points in the fitted region. Figures of merit for these fits are $\chi^2_\nu = 15.8$ and R=0.006. For a definition of these figures of merit see ref. 7

Although we show here fitting results for a Ni-doping level of $y = 0.06$, no significant differences were found in the fitted values for the lower Ni dopings. The Ni-O(2) apical distance is 0.16(1) Å shorter than the corresponding Cu-O(2) apical distance.

TABLE 1. Selected fit results at the Ni K-edge. Data corresponds to $y = 0.06$ at T=10K; $S_0^2 = 0.902 \pm 0.067$. Diffraction results are from Radelli $et.\ al$ [6].
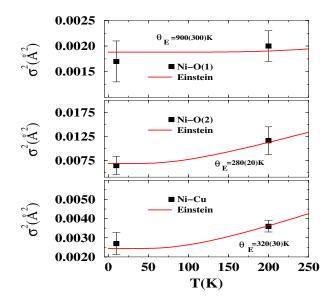
	XAFS	Diffraction
Ni-O(1)	1.882(8) Å	1.88773 Å
Ni-Cu	3.789(6) Å	3.7736 Å
Ni-O(2)	2.250(12) Å	2.4145 Å
Ni-La$_c$	4.701(16) Å	4.7604 Å

The Ni-O(1) planar distance is nearly unchanged relative to the Cu-O(1) distance, although a relative expansion of the former by $\lesssim 0.01$ Å cannot be ruled out based on the slightly larger Ni-Cu planar distance and the measured uncertainties. Ni-O(1)-Cu MS paths contribute to the XAFS at nearly the same distance as Ni-Cu single scattering (SS) paths and are included in the fits. As the O(2)-apical moves towards Ni it drags along its neighbor La atom, as seen by the ≈ 0.06 Å contraction in Ni-La$_c$ distance. Ni-O(2)-La$_c$ MS paths contribute at nearly the same distance as Ni-La$_c$ SS paths and are included in the fits.

The buckling angle α of the Ni-O(1)-Cu planar, nearly collinear, configuration was determined by fitting a parameterized form of the effective scattering amplitudes of double and triple scattering paths, $F_k(\alpha)$, to the data. The parameterization was done by simulating the buckling angle dependence of such amplitudes in FEFF6 calculations (for a detailed description of this procedure see ref. 5). The fitted value of $\alpha = 2.5 \pm 3°$ is in agreement with the average buckling angle determined by diffraction, $\langle \alpha \rangle = 3.61°$, indicating again that the structural disorder introduced by Ni in the CuO$_2$ planes is small. The large uncertainty in buckling angle α is due to the small variation of $F_k(\alpha)$ for small buckling angles near collinearity ($0 \leq \alpha \leq 5°$).

Whether there is a spatial correlation between the positions of the two types of dopants (Ni,Sr) can be determined from Ni K-edge XAFS by fitting the Ni-(La/Sr) XAFS signal with varying amounts of (Sr/La) neighbors to Ni. Sr and La have very different backscattering amplitudes making plausible separating their isolated contributions to the XAFS. A fit to the Ni-(La/Sr) signal determines a relative Sr concentration of $x = 0.048 \pm 0.06$. For a random solution one expects $x = 0.075$, while if Sr avoids Ni one expects $x = 0$. Unfortunately the fitted value is consistent with either one of these scenarios. However, we can definitely rule out a tendency of Sr to occupy sites near Ni atoms. We note that determining the Sr-Ni correlation from Sr K-edge XAFS is not possible, due to the nearly identical backscattering amplitudes of Ni and Cu atoms.

Fitted values for the mean-squared disorder in selected interatomic distances at T=10, 200K together with their parameterization to an Einstein model are shown in Fig. 6. We found no evidence for a static contribution to the mean-squared disorder in these distances. The much weaker effective force constant of the Ni-
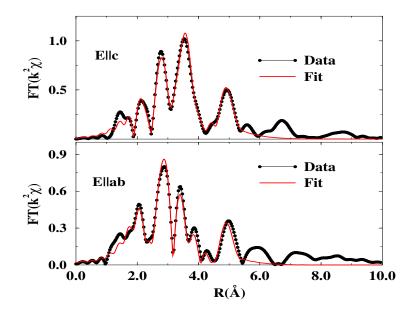
FIGURE 6. Temperature dependence of the mean-squared disorder in selected interatomic distances around Ni atoms together with their fits to Einstein models. The mean-squared disorder in these bonds is solely of thermal origin without any evidence for a static contribution.
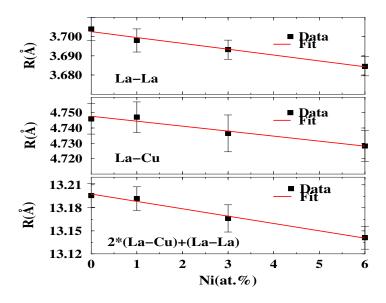
O(2) apical bond compared to that of Ni-O(1) planar bond is evident from the much larger temperature dependence of the former. This weaker bonding allows the O(2) apical to relax towards the Ni^{+2} ion while the strongly covalent Ni-O(1) bonding opposes the relaxation of O(1) atoms, thus preventing a true *anti-Jahn-Teller* distortion at the Ni site to materialize, as discussed below.

The XANES spectra shown in Fig. 4 fully support the XAFS results regarding the distortion of the NiO_6 octahedra. The ratio of the out-of-plane, Ni-O(2) apical distance, to the in-plane, Ni-O(1) distance, $R = r_{\parallel}/r_{-}$, determines the $4p_{\pi}$-$4p_{\sigma}$ energy splitting shown in Fig. 4. This is because the energy of a $4p_{\pi}3d^9\underline{L}$ ($4p_{\sigma}3d^9\underline{L}$) final state scales as $1/r_{\parallel}^2$ ($1/r_{-}^2$). Here $\underline{L}$ denotes a ligand shell hole which is created by transfering a ligand shell electron to the $3d$-shell in order to screen the core-hole in the excited final state. The assignment of the XANES features to the above mentioned final state configurations is based on extensive studies of La-cuprates and La-nickelates by Oyanagi *et al.* [9], Kosugi *et al.* [10] and Sahiner *et al.* [11]. Sahiner *et al.* summarized the measured $4p_{\pi}$-$4p_{\sigma}$ energy splitting for a series of cuprates and nickelates with known octahedral distortions. This splitting varies linearly with the distortion parameter $1/R^2$ [11]. By interpolating our measured splitting of 3.0 eV into their curve we obtain a distortion parameter $1/R^2 = 0.71$ or $R = r_{\parallel}/r_{-} = 1.19$. This is in excellent agreement with the XAFS result of $R = 1.19(1)$.

Fits to La K-edge XAFS data are shown in Fig. 7. The local $\hat{c}$-axis, as obtained by averaging over all La sites, is given by the sum $2\times$(La-Cu_c)+ (La-La_c), where (La-Cu_c) and (La-La_c) bonds are nearly coincident with the c-axis. Figure 8 shows the rate of contraction of the local $\hat{c}$-axis with Ni-doping, at T=10K. This rate is
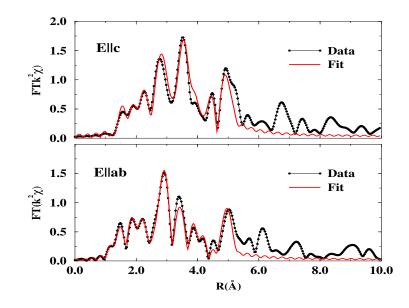
FIGURE 7. Magnitude of complex Fourier transform of $k^2\chi(k)$ for La K-edge at T=10K and $y = 0.06$. Data range used in the transform is $[3,14]\,\text{Å}^{-1}$. The constrained fit of both orientations uses 22 fitting parameters compared to 52 independent points in the fitted region. $S_0^2 = 0.93(6)$; figures of merit are $\chi_\nu^2 = 14.89$, R=0.008 .

FIGURE 8. Ni-induced contraction of the local $\hat{c}$-axis, averaged over all La sites, at T=10K. The rate of contraction is in good agreement with the macroscopic $\hat{c}$-axis contraction determined from powder diffraction measurements at 300K. $y = 0$ results are from ref. 12.

found to be $(dc/dy)_{10\text{K}} = -0.0095(25)[\,\text{Å}/\text{at. }\%\text{Ni}]$. This is comparable to the measured contraction rate at T=300K found from our powder diffraction measurements (fig. 1); i.e., $(dy/dc)_{300\text{K}} = -0.0080(5)[\,\text{Å}/\text{at. }\%\text{Ni}]$.
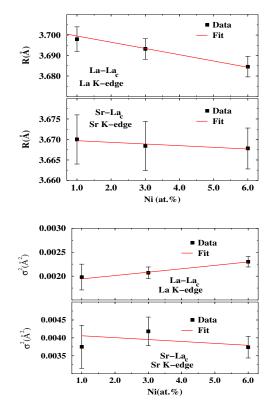
FIGURE 9. Magnitude of complex Fourier transform of $k^2\chi(k)$ for Sr K-edge at T=10K and $y = 0.06$. Data range used in the transform is [3,14] Å^{-1}. The constrained fit of both orientations uses 22 fitting parameters compared to 52 independent points in the fitted region. $S_0^2 = 1.08(10)$; figures of merit are $\chi_\nu^2 = 15.6$, R=0.022 .

Fits to Sr K-edge data are shown in Fig. 9. While the measured La-O(2) apical distance determined from La XAFS, $r = 2.36(1)$ Å, agrees with the value of crystallography [6] for the undoped structure (i.e., $y = 0$), $r = 2.354$ Å, the local Sr-O(2) apical distance is determined from the Sr K-edge analysis to be $r = 2.45(2)$ Å. In addition, Sr-distances along the $\hat{c}$-axis show a different response to Ni-doping than that found at the La sites. This is shown in figs. 10- 11 where the Ni-doping dependence of (La/Sr)-La$_c$ and (La/Sr)-(Cu/Ni)$_c$ distances and their mean-squared disorder, as obtained from La and Sr XAFS analysis, are shown. It is clear that the Sr distances along the $\hat{c}$-axis are less affected by the Ni substitution.

DISCUSSION

The local contraction of NiO$_6$ octahedra derived from the Ni XAFS and XANES measurements is driven by the non-Jahn-Teller nature of a Ni^{+2}-ion in its 3d^8, high-spin, electronic configuration. This is schematically illustrated in fig. 12, where the octahedral distortions measured by crystallography around Ni in undoped-La$_2$NiO$_4$ and around Cu in undoped-La$_2$CuO$_4$ are shown together with the electronic population/splitting of the 3d$_{x^2-y^2}$ and 3d$_{3z^2-r^2}$ energy levels in the e_g manifold. Since both cuprates and nickelates have a tetragonal crystal structure, this crystal field lifts the degeneracy of the e_g manifold. The *pseudo-Jahn-Teller* effect in La$_2$CuO$_4$ (Cu^{+2}, 3d^9 configuration) arises due to the difference in population between 3d$_{x^2-y^2}$ and 3d$_{3z^2-r^2}$ energy levels; i.e., it is convenient to elongate the octahedron along
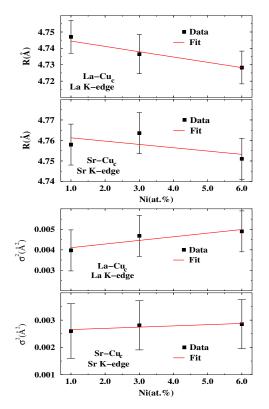
FIGURE 10. Ni-doping dependence of the (La/Sr)-La$_c$ distances (top) and mean-squared disorder (bottom) determined from La and Sr K-edge XAFS analysis. The La-distances respond more strongly to Ni-doping than the Sr-distances.

the $\hat{c}$-axis (lower the energy of the doubly populated $3d_{3z^2-r^2}$ states) while compressing it in the plane (raising the energy of the singly populated $3d_{x^2-y^2}$ state by the same amount). The energy advantage in having a spontaneous elongation of the octahedra disappears in a Ni^{+2} ($3d^8$) ion in its high-spin state since the occupation of $3d_{x^2-y^2}$ and $3d_{3z^2-r^2}$ e_g levels is the same. The disappearance of the Jahn-Teller distortion is a direct proof of a divalent, high-spin Ni ion since a Ni^{+3} state ($3d^7$) or a Ni^{+2} low-spin state, would have resulted in measurable Jahn-Teller distortions. These findings severely limit models of T$_c$ suppression which invoke trapping of doped holes by Ni, as that would imply a Ni^{+3} state, inconsistent with our measurements.

It is interesting to compare the NiO$_6$ octahedral distortion with that in pure La$_2$NiO$_4$. In the latter, a fully relaxed non-Jahn-Teller Ni^{+2} ion results in a Ni-O(1) planar distance ≈ 0.04 Å longer than the Cu-O(1) distance in JT-distorted La$_2$CuO$_4$ (despite Ni^{+2} being a smaller ion than Cu^{+2}). Similarly, the Ni-O(2) apical distance is ≈ 0.18 Å shorter than the Cu-O(2) one (fig. 12).
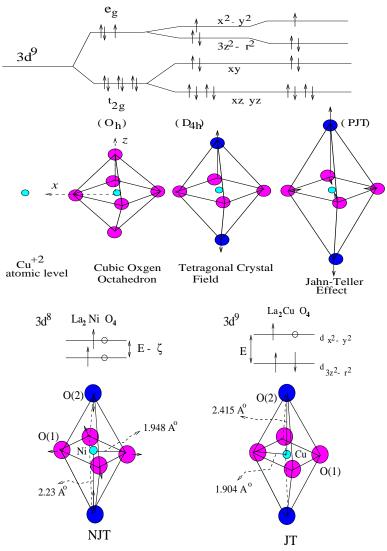
Our measurements indicate that although the $\hat{c}$-axis contraction of Ni-O(2) in La$_{1.85}$Sr$_{0.15}$Cu$_{1-y}$Ni$_y$O$_4$ is consistent with an almost fully-relaxed non-Jahn-Teller state (≈ 0.16 Å), the in-plane Ni-O(1) distance does not elongate by more than

FIGURE 11. Ni-doping dependence of the (La/Sr)-Cu$_c$ distances (top) and mean-squared disorder (bottom) determined from La and Sr K-edge XAFS analysis. The La-distances respond more strongly to Ni-doping than the Sr-distances.

0.01 Å. The most likely explanation for this is that the NiO$_6$ octahedra are embedded in the very rigid, highly covalent, CuO$_2$ planes, which prevents the in-plane Ni-O(1) distance from significantly expanding and deforming the surrounding CuO$_2$ network. The larger temperature dependence in mean-squared disorder of Ni-O(2) distance compared to Ni-O(1) is supportive of this notion. The softer Ni-O(2) bond can therefore contract without resulting in a significant elastic energy cost. The above arguments imply that a fully relaxed non-Jahn-Teller state is not materialized for Ni in La$_{1.85}$Sr$_{0.15}$Cu$_{1-y}$Ni$_y$O$_4$.

The larger response of La-La$_c$ and La-(Cu/Ni)$_c$ distances than Sr-La$_c$ and Sr-(Cu/Ni)$_c$ to Ni-doping can be understood in more than one way. One possibility is that Sr enters the lattice away from Ni sites and therefore is less sensitive to the enhanced local lattice deformation around Ni sites. As mentioned earlier, the fit results of the Ni-(Sr/La) XAFS signal are consistent with such hypothesis, due to the large uncertainty in the relative weight of La/Sr neighbors to Ni. Why would Sr avoid Ni? In a previous XAFS study of La$_{2-x}$Sr$_x$CuO$_4$ for a series of x-values below and above the insulator-metal (I-M) transition ($x \approx 0.06$ at T=10K), we detected a response of the Sr-O(2) apical distance to the delocalization of doped hole-carriers while no such response was found for the La-O(2) apical distance [13]. This testifies

FIGURE 12. Top: schematic illustration of the electronic origin of the Jahn-Teller effect for a Cu^{+2} ion in an octahedral environment. The e_g and t_{2g} manifolds are split by the tetragonal crystal field and the pseudo-Jahn-Teller effect enhances the tetragonal distortion. Bottom: measured octahderal distortions in pure La_2NiO_4 and La_2CuO_4. The NiO_6 octahedral distortion in $La_{1.85}Sr_{0.15}Cu_{1-y}Ni_yO_4$ is very similar to that in pure La_2NiO_4, except that the rigid CuO_2 plane prevents a significant Ni-O(1) in-plane distortion to materialize. Sr doping contracts the Cu-O(1) distance in $La_{2-x}Sr_xCuO_4$ [6].

to the fact that doped-holes introduced by the Sr-dopants are sharply peaked in the vicinity of the Sr in the insulating phase while becoming more extended in the metallic phase. It is reasonable to argue that, if the I-M transition is caused by increased overlap of impurity states, the extended impurity states will remain peaked in the vicinity of the Sr even in the metallic state. A similar conclusion was reached by Hammel *et al.* in their nuclear quadrupole resonance study of

$La_{2-x}Sr_xCuO_4$ [14].

It follows that if Sr likes to keep the doped-holes in its neighborhood due, e.g., to their attraction to the Sr^{+2} impurity potential, and, *if* Ni prefers to avoid them, a correlation in Ni-Sr positions could arise. It is clear that doped holes will be scattered strongly from the potential introduced by the local distortion around Ni. In fact doped-holes become localized with Ni-doping at $y \approx 0.05$ [4]. Our observation of a Ni^{+2}, $3d^8$ high-spin state for Ni even at $y = 0.06$ indicates that the doped holes are not localized at Ni sites. The localization of carriers at $y \approx 0.05$ must occur away from Ni sites. It could be that Ni "repels" holes to preserve its high-spin state and associated Hund's exchange energy.

An alternative explanation for the observed differences between Sr and La sites is the much weaker bonding between the O(2)-apical and a Sr^{+2} ion compared to a La^{+3} ion. The measured Sr-O(2) apical distance (longer by $\approx 0.1 \, \text{Å}$) is a result of the much weaker Madelung potential felt by the negatively charged O(2) apical oxygen near a Sr ion, resulting in an equilibrium position further away from the Sr and closer to the CuO_2 planes. Such distortion was already reported in a previous study of $La_{2-x}Sr_xCuO_4$ [13]. When NiO_6 octahedra contract and the O(2) ion is displaced towards Ni, the La^{+3} ions follow the O(2) displacement, due to a significant degree of covalency in the La-O(2) bonding (the La-O(2) apical distance, $2.35 \, \text{Å}$, is shorter than expected for a purely ionic bond). That La follows the O(2) apical is clearly seen by the measured contraction in Ni-La$_c$ distance (table 1) and in the Ni-induced contraction of the La-(Cu/Ni)$_c$ distance (fig. 11). However, since Sr ions are weakly bound to O(2) apicals, they might not follow the O(2) apicals in their journey towards the Ni ions in the contracted NiO_6 octahedra, resulting in a much smaller change in the Sr-(Cu/Ni)$_c$ distance relative to La-(Cu/Ni)$_c$ distance. A similar effect can also explain the behavior of La/Sr-La$_c$ distances. This explanation does not require a deviation from randomness in the solid solution.

Despite having a magnetic moment, Ni suppresses T_c at a similar rate (albeit smaller) than non-magnetic Zn. Zn doping in $La_{2-x}Sr_xCuO_4$ is expected to manifest a similar ZnO_6 octahedral distortion, as a filled-shell, Zn^{+2} $3d^{10}$ ion is also a non-Jahn-Teller ion. The very similar macroscopic $\hat{c}$-axis contraction observed for both dopants supports this notion. It is not clear how the local distortion around Ni would contribute to pair breaking, but it is reasonable to assume that doped holes will scatter strongly from such distorted centers. This scattering will modify the spatial distribution of hole carriers. If these hole carriers reside predominantly in the CuO_2 planes, their wavefunctions will be peaked in between Ni ions. The spatial extent of a superconducting state cannot be confined to a region smaller than its coherence length, as the resulting quasi-particle localization energy would be larger than the superconducting energy gap. It is interesting to note that T_c is completely suppressed at 3-4 at. % Ni, where the average distance between Ni dopants in the two-dimensional CuO_2 planes is $3.78/\sqrt{y} = 19 - 22 \, \text{Å}$. This is about the size of the in-plane superconducting coherence length, $\zeta_{ab} = 22.7 \, \text{Å}$ for $La_{1.85}Sr_{0.15}CuO_4$ [15].

It is then possible that superconductivity is destroyed when the doped holes are constrained to occupy regions of the CuO_2 plane in between Ni centers, which, for $y \geq 0.04$, are smaller than ζ_{ab}.

CONCLUSIONS

New tools are becoming available that allow imaging and spectroscopy of high T_c superconductors at the atomic level. Scanning tunneling microscopy, e.g., has already proven to be a powerful technique for unraveling some important details about the spatial symmetry and extent of impurity states around Zn dopants in a high T_c superconductor. Such experiments are bringing us closer to determining the symmetry of the superconducting order parameter. These new techniques can only be fully exploited if a quantitative understanding of the local structure at the atomic level is available. This is particularly important for dopants, where the local structure typically differs from the macroscopic structure.

We have shown here that a strong lattice distortion exists around the Ni atoms in $La_{1.85}Sr_{0.15}Cu_{1-y}Ni_yO_4$. This distortion manifests a large $\hat{c}$-axis contraction of the NiO_6 octahedra, which propagates to higher shells of neighboring atoms along the $\hat{c}$-axis. This has implications for the interpretation of spectroscopies that are sensitive to spatially-inhomogeneous local $\hat{c}$-axis distortions. For example, the local tunneling cross sections, which depend on the local inter-layer spacing, will vary from a (Ni/Zn) dopant site to a neighboring Cu site due to the local $\hat{c}$-axis fluctuations.

Enhanced scattering of the doped holes by the NiO_6 octahedral distortions will likely result in an inhomogeneous charge distribution of the doped holes, with hole-poor regions around Ni dopants. This is somewhat different than the "swiss cheese" model of Nachumi *et al.*, in that it implies an inhomogeneous hole distribution in the *normal* state, leading to a spatially inhomogeneous superconducting order parameter below T_c. The "swiss cheese" model predicts a uniform normal state charge distribution and the effect of dopants is to remove superconducting pairs from the superfluid in a $\pi\zeta_{ab}^2$ region around the dopants. Superconductivity is fully suppressed when the average distance between Ni dopants is on the order of the in-plane superconducting coherence length. This is expected if charge carriers are confined to the regions in between Ni dopants, as the spatial extent of a superconducting state cannot be confined to a region smaller than its coherence length.

The Sr and La environments respond differently to Ni doping. Although this could be explained as due to Ni entering the lattice away from Sr sites, a more likely explanation involves a weak Sr-O(2) apical bond compared to a stronger La-O(2) apical bond. The latter results in La ions "following" the O(2) apical distortion toward Ni ions, while the Sr ions are not much affected due to their weak link to the O(2) apicals.

ACKNOWLEDGMENTS

REFERENCES

1. S. H. Pan, E. W. Hudson, K. M. Lang, H. Eisaki, S. Uchida and J. C. Davis, Nature **403**, 746 (2000).
2. J. M. Byers, M. E. Flatte and D. J. Scalapino, Phys. Rev. Lett. **71**, 3363 (1993).
3. A. V. Balatsky, Nature **403**, 717 (2000).
4. M. Z. Cieplak, S. Guha, H. Kojima, P. Lindenfeld, G. Xiao, J. Q. Xiao and C. L. Chien, Phys. Rev. B **46**, 5536 (1992).
5. D. Haskel, E. A. Stern, F. Dogan and A. R. Moodenbaugh, Phys. Rev. B **61**, 7055 (2000).
6. P. G. Radaelli *et al.* , *Phys . Rev. B.* **49**, 4163 (1994).
7. E. A. Stern, M. Newville, B. Ravel, Y. Yacoby and D. Haskel, Physica B **208& 209**, 117 (1995).
8. S. I. Zabinsky, J. J. Rehr, A. Ankudinov, R. C. Albers and M. J. Eller, Phys. Rev. B **52**, 2995 (1995).
9. H. Oyanagi, Y. Yokoyama, H. Yamaguchi, Y. Kuwuahara, Katayama and Y. Nishihara, Phys. Rev. B **42**, 10136 (1990).
10. N. Kosugi, Y. Tokura, H. Tajima and S. Uchida, Phys. Rev. B **41**, 131 (1990).
11. A. Sahiner *et al.*, Phys. Rev. B **51**, 5879 (1995).
12. D. Haskel, Ph. D Thesis, University of Washington, 1998.
13. D. Haskel, E. A. Stern and F. Dogan, in *Phase transitions and self organization in electronic and molecular networks*, to appear in *Fundamental Materials Research* series, edited by M. F. Thorpe and J. C. Phillips.
14. P. C. Hammel, B. W. Statt, R. L. Martin, F. C. Chou, D. C. Johnston and S. W. Cheong, Phys. Rev. B **57**, R712 (1998).
15. M. E. Nachumi *et al.*, Phys. Rev. Lett. **77**, 5421 (1996).